



HAL
open science

Endovascular Magnetically-Guided Robots: Navigation Modeling and Optimization

Laurent Arcèse, Matthieu Fruchard, Antoine Ferreira

► **To cite this version:**

Laurent Arcèse, Matthieu Fruchard, Antoine Ferreira. Endovascular Magnetically-Guided Robots: Navigation Modeling and Optimization. *IEEE Transactions on Biomedical Engineering*, 2012, 54 (4), pp.977 - 987. 10.1109/TBME.2011.2181508 . hal-00655583

HAL Id: hal-00655583

<https://hal.science/hal-00655583>

Submitted on 31 Dec 2011

HAL is a multi-disciplinary open access archive for the deposit and dissemination of scientific research documents, whether they are published or not. The documents may come from teaching and research institutions in France or abroad, or from public or private research centers.

L'archive ouverte pluridisciplinaire **HAL**, est destinée au dépôt et à la diffusion de documents scientifiques de niveau recherche, publiés ou non, émanant des établissements d'enseignement et de recherche français ou étrangers, des laboratoires publics ou privés.

Endovascular Magnetically-Guided Robots: Navigation Modeling and Optimization

Laurent Arcese, Matthieu Fruchard, Antoine Ferreira

Abstract—This paper deals with the benefits of using a nonlinear model-based approach for controlling magnetically guided therapeutic microrobots in the cardiovascular system. Such robots used for minimally invasive interventions consist of a polymer binded aggregate of nanosized ferromagnetic particles functionalized by drug-conjugated micelles. The proposed modeling addresses wall effects (blood velocity in minor and major vessels' bifurcations, pulsatile blood flow and vessel walls, and effect of robot-to-vessel diameter ratio), wall interactions (contact, van der Waals, electrostatic and steric forces), non-Newtonian behaviour of blood and different driving designs as well. Despite nonlinear and thorough, the resulting model can both be exploited to improve the targeting ability and be controlled in closed-loop using nonlinear control theory tools. In particular, we infer from the model an optimization of both the designs and the reference trajectory to minimize the control efforts. Efficiency and robustness to noise and model parameter's uncertainties are then illustrated through simulations results for a bead pulled robot of radius $250\mu\text{m}$ in a small artery.

Index Terms—Endovascular navigation, magnetic steering, nonlinear modeling, optimal trajectory, nonlinear controller and observer.

I. INTRODUCTION

Emerging real-time high spatial resolution medical imagers, using either computed tomography [1], optical coherence tomography or Magnetic Resonance Imaging (MRI) devices [2], [3], are promising for the development of automated medical interventions. In particular, it opens a wide field in minimally invasive diagnostic, therapy or *in-vivo* biosensing. Deflected ferromagnetic catheters [4] or unthetered capsule [5] are already used for medical interventions at the millimeter scale. Recent developments in nanotechnology have allowed the exploration of robots capable of propulsion at the micro and nano scale. One of the primary challenges are the locomotion and power at these scales. Since the smallest adequate motors are some hundreds micrometers long, embedded actuation does not seem to be a suitable choice for artificial robots swimming in the blood flow. Furthermore, traditional onboard power supplies, i.e batteries, cannot be scaled at these dimensions.

Two main approaches have been proposed to solve this issue using harvesting energy from the biological environment and an externally energy field. The first approach employs chemical locomotion to harvest energy from chemicals in the

environment such as H_2O_2 [6]. Magnetotactic bacteria actuated thanks to embedded ferromagnetic material has also been demonstrated [7]. To date the most systematically approach uses wireless power transmission through magnetic fields [4], [8]. Different designs have been proposed in the literature for such microrobots with distinguishing physical features [9]. A first propulsion scheme is biologically inspired using either Helical Tail (HT) [10], [11], beating flagella [12], or Elastic Flagella (EF) [13], [14]; a second one is referred as Bead Pulling (BP) [15], [16]. Actually, the most advanced design relies on bead pulling [17] since *in-vivo* experiments were conducted in the carotid artery of a living swine [18].

All these contributions emphasize the difficulties of controlling magnetic microrobots in fluids through magnetic fields actuation. Achieving motion control of magnetic microrobot necessitates nonlinear dynamics modeling and analysis [19], [20], [21]. Some models are very precise and thorough but rely on finite or discrete elements methods [22]: while these studies are useful to predict the microrobot's trajectory, they are awkward for parametric analysis and their high computational costs are not compatible with *on-line* control purposes and experiments. At the opposite, most of the literature dedicated to the control of magnetically-guided microrobots neglects wall effects and interactions. These studies mainly address the control of linearized models. Thus, stability and robustness issues, pointed out by the authors in [23], [24], could have been expected.

On top of dealing with the nonlinearities of the model, control approaches have to solve some actuators sizing problems [22], [25] due to both limitations on actuators and the increasing prevalence of blood flow drag over magnetic force as the robot navigates in smaller vessels [26]. In [17] and [22], the authors show that an optimal robot-to-vessel diameter ratio should be respected so as to minimize the drag force prevalence. Hence, designing the microrobot as a degradable binded aggregate of magnetic nanoparticles can be a technological way to navigate in smaller vessels.

The present paper addresses the benefits of using a nonlinear model-based approach for designing and controlling a magnetically-guided functionalized microrobot in the blood flow, especially at vessel bifurcations (see Figure 1). The contribution is threefold. First, in Section II, we give a precise forces balance, which includes wall effects (bifurcations, pulsatile blood flow), wall interactions (contact, van der Waals, electrostatic, and steric forces induced by the robot's functionalization) and non-Newtonian behaviour of blood. In particular, we address the modeling of bifurcation effects (minor and major ones) using analytical approximations of Computational Fluid Dynamics (CFD) simulations. We also address the design of nonlinear observer and controller that

This work was supported by European Union's 7th Framework Program and its research area ICT-2007.3.6 Micro/nanosystems under the project NANOMA (Nano-Actuators and Nano-Sensors for Medical Applications).

L. Arcese and M. Fruchard are with the Laboratoire PRISME University of Orleans, IUT de Bourges, 63 Av de Latre de Tassigny, 18020, Bourges cedex, France laurent.arcese@bourges.univ-orleans.fr matthieu.fruchard@bourges.univ-orleans.fr

A. Ferreira is with the Laboratoire PRISME Ecole Nationale Supérieure d'Ingénieurs de Bourges, 88 Bd Lahitolle, 18000, Bourges, France antoine.ferreira@ensi-bourges.fr

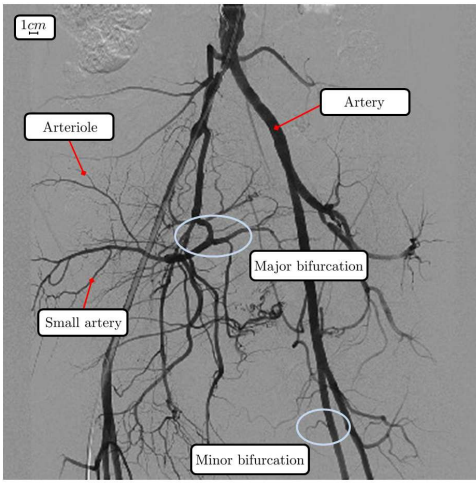


Fig. 1. Complexity of endovascular navigation for a magnetic microrobot from macro to micro-vasculature.

guarantee the stability of the tracking along any navigation trajectory. Section III-A is then devoted to the exploitation of the proposed nonlinear modeling to optimize both the design and the reference trajectory that the microrobot should track in the macro and micro-vasculature. In particular, we show that the optimal size for different swimming methods (BP, EF and HT designs) should not be as big as expected in [17] due to the influence of wall interactions. The navigation can also be optimized so as to minimize the control efforts. These two results suggest that embolization hazards can be reduced while improving the targeting of medical interventions. In Section III-C, simulation results illustrate the performances and robustness to noise measurements and parametric errors of the proposed approach in a small artery, with concerns about the limitations of a clinical MRI gradient coils. Finally, we discuss some open issues in Section III-D and conclude in Section IV.

II. METHODOLOGY

A. Analytical model

Let consider a spherical ferromagnetic microrobot, of radius r , immersed in blood vessels. The microrobot is governed by several forces including a magnetic motive force \vec{F}_m , the blood hydrodynamic drag force \vec{F}_d , the microrobot's apparent weight \vec{W}_a , the contact force \vec{F}_c , the van der Waals and the electrostatic interaction forces, \vec{F}_{vdw} and \vec{F}_{el} , between the microrobot and the vessel walls and finally the steric interaction force \vec{F}_s between the robot's polymer chains and the endothelial glycocalyx. The Knudsen number is large enough to neglect the effect of Brownian motion. The translational motion of a robot of mass m is given by:

$$m \frac{d\vec{v}}{dt} = \vec{F}_m + \vec{F}_d + \vec{W}_a + \vec{F}_c + \vec{F}_{vdw} + \vec{F}_{el} + \vec{F}_s \quad (1)$$

where \vec{v} is the translational velocity of the robot.

1) *Motive force:* Three main schemes of magnetically actuated microrobots have been developed (see Figure 2), namely bead pulled, elastic flagellated, and helical tailed robots. The motive force \vec{F}_m for each class of robot is detailed hereinafter.

- Bead pulling (BP) approach relies on the use of magnetic gradient coils for propulsion. The magnetic gradient induces a magnetic motive force \vec{F}_m on the robot (see Figure 2(a)):

$$\vec{F}_m = \tau_m V (\vec{M} \cdot \nabla) \vec{B} \quad (2)$$

where V and V_m are the robot's and the ferromagnetic volumes, $\tau_m = \frac{V_m}{V}$, and \vec{M} is the bead's magnetization, $\nabla \vec{B}$ is the magnetic gradient. Within an MRI device, the orientation of the robot does not change due to the magnetic torque $\vec{\Gamma}_m$ which tends to align the robot's magnetization \vec{M} along the MRI uniform magnetic field $B_0 = 3T$, which also ensures a saturation magnetization M_{sat} .

- Biologically inspired flagellated robots (see Figure 2(b)) have been designed through various concepts, see [9] for a survey. In magnetically-driven Elastic Flagellated propulsion (EF), the wave motion of the elastic tail is induced by the magnetic torque applied on the attached magnetic bead:

$$\vec{\Gamma}_m = \tau_m V \vec{M} \times \vec{B} \quad (3)$$

With an oscillating magnetic input \vec{B} of norm B_0 at frequency ω , the post-transient resulting motive torque has an amplitude $\gamma_0 = \tau_m V \|\vec{M}\| B_0$. For small-amplitude motion (under assumption that $\frac{\gamma_0 L}{k_\kappa} \ll 1$), the elasto-hydrodynamics are described by an hyperdiffusion equation and the resulting motive force is given by [14]:

$$\vec{F}_m = \frac{\omega \zeta_\perp \gamma_0^2 L^4}{4k_\kappa^2} Z(S_p) \frac{\langle \vec{B} \rangle}{\| \langle \vec{B} \rangle \|} \quad (4)$$

where L , $\zeta_\perp = \frac{4\pi\eta}{\ln \frac{L}{2\kappa} + 0.193}$ and $\kappa \ll r$ are respectively the length, the normal viscous drag coefficient, and the radius of the flagellum. $k_\kappa = \frac{\pi E_\kappa \kappa^4}{4}$ denotes the bending stiffness of the tail, $\langle \cdot \rangle$ denotes the time average operator over one period, and Z is a scaling function dependent on the Sperm number $S_p = \left(\frac{L^4 \omega \zeta_\perp}{k_\kappa} \right)^{1/4}$. The latter is a decreasing function of S_p , valid only for $S_p \geq 3.4$ [14].

It should be noticed that more effective concepts have been proposed, e.g. planar wave flagellated robot [27], where the increased efficiency requires a distributed actuation.

- The rotating magnetic torque (3) can also be exploited to generate a corkscrew effect for a bead attached to an helical tail (HT) illustrated by Figure 2(c). The post-transient motive force is given by [26]:

$$\vec{F}_m = 2\pi n r [r \cos \varphi (\zeta_\perp - \zeta_\parallel) \omega \frac{\vec{F}_m}{\|\vec{F}_m\|} - \frac{\zeta_\perp \sin^2 \varphi + \zeta_\parallel \cos^2 \varphi}{\sin \varphi} (\vec{v} - \vec{v}_f)] \quad (5)$$

where φ and n are the pitch angle and the number of helical turns, \vec{v} and \vec{v}_f respectively denote the robot's and the fluid's velocity. The viscous drag coefficients for flows respectively normal and parallel to the tail's axis are given by:

$$\zeta_\perp = \frac{4\pi\eta}{\ln \frac{0.36\pi r}{\kappa \sin \varphi} + 0.5} > \zeta_\parallel = \frac{2\pi\eta}{\ln \frac{0.36\pi r}{\kappa \sin \varphi}} \quad (6)$$

In (5), the first term is a pure driving force resulting from the corkscrew effect, and the second term is a slow down force induced by the drag exerting on the tail.

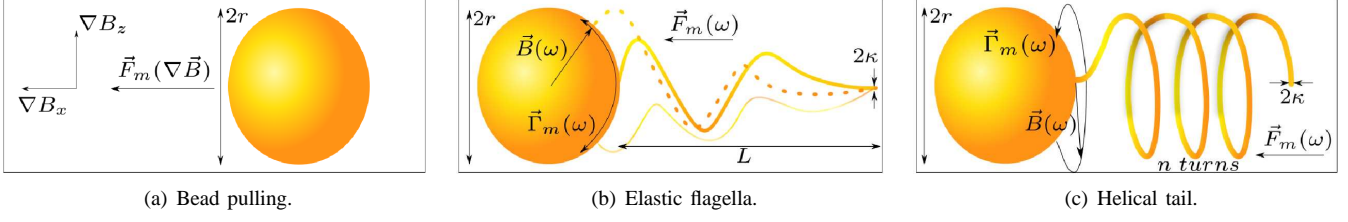


Fig. 2. Different microrobots designs. (a) Bead pulling: control input is the magnetic gradient $\nabla\vec{B}$. (b) Elastic flagella: control inputs are the time-average magnetic field direction and the frequency. (c) Helical tail: control inputs are the magnetic torque direction and the frequency.

2) *Hydrodynamic drag force*: Hydrodynamics effects are classically modeled using the Navier-Stokes equation, whose analytical solution is lacking. A numerical approach implies time-consuming computations, that are not compatible with real-time approaches. Assuming that the fluid is incompressible, the drag force exerted on a sphere is approximated by:

$$\vec{F}_d = -\frac{1}{2}\rho_f(\vec{v} - \vec{v}_f)_\infty^2 AC_{d\infty} \frac{(\vec{v} - \vec{v}_f)_\infty}{\|(\vec{v} - \vec{v}_f)_\infty\|} \quad (7)$$

where ρ_f denotes the fluid density, A is the robot's frontal area, and C_d is the R_e -dependent drag coefficient; for a sphere in a fluid of infinite extent in laminar flow, we have:

$$C_{d\infty} = \frac{24}{R_{e\infty}} + \frac{6}{1 + \sqrt{R_{e\infty}}} + 0.4, \quad R_{e\infty} = \frac{2r\rho_f\|\vec{v} - \vec{v}_f\|_\infty}{\eta} \quad (8)$$

• *Non-Newtonian fluid*. In the case of blood, the fluid's viscosity η depends both on the vessel's diameter d (in $10^{-6}m$) and on the hematocrit rate h_d (see Figure 3) according to the three following empirical relations [28]:

$$\eta = \frac{\eta_{pl}d^2}{(d-1.1)^2} \left[1 + \frac{(\eta_{0.45}-1)d^2}{(d-1.1)^2} \frac{(1-h_d)^c - 1}{(1-0.45)^c - 1} \right] \quad (9)$$

with parameters η_{pl} and $\eta_{0.45}$ denoting respectively the plasma viscosity and the relative apparent blood viscosity for a fixed discharge hematocrit of 0.45, given by:

$$\eta_{0.45} = 6e^{-0.085d} + 3.2 - 2.44e^{-0.06d^{0.645}}$$

The shape of the viscosity dependence on hematocrit is:

$$c = \frac{10^{11}}{d^{12}} - (0.8 + e^{-0.075d}) \left(\frac{d^{12}}{d^{12} + 10^{11}} \right)$$

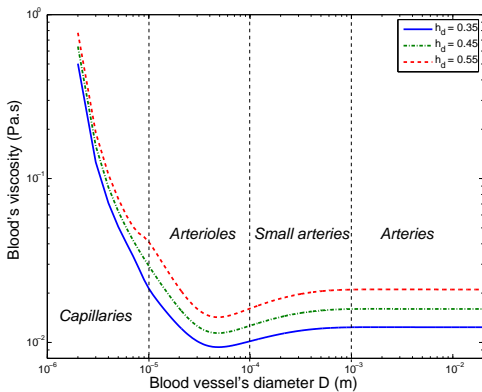


Fig. 3. Blood viscosity exhibits non-Newtonian behaviour in smaller vessels.

• *Wall effects*. Equation (7) neglects wall effects, which has to be corrected considering the impact of the vessel walls on the robot's velocity for endovascular applications. This wall effect is commonly expressed as a ratio between the terminal relative velocity of the robot $(\vec{v} - \vec{v}_f)$ and its velocity $(\vec{v} - \vec{v}_f)_\infty$ in an infinite extent of fluid [29]:

$$\frac{\|\vec{v} - \vec{v}_f\|}{\|(\vec{v} - \vec{v}_f)_\infty\|} = \frac{1 - \lambda^{\alpha_0}}{1 + \left(\frac{\lambda}{\lambda_0}\right)^{\alpha_0}} \quad (10)$$

with diameter ratio $\lambda = 2r/D$ and D denoting the vessel diameter (in m). Parameters α_0 and λ_0 are functions of Reynolds number, but are commonly set to 1.5 and 0.29, respectively. Thus, equation (7) becomes:

$$\vec{F}_d = -\frac{\rho_f}{2} \left[\frac{1 + \left(\frac{\lambda}{\lambda_0}\right)^{\alpha_0}}{1 - \lambda^{\alpha_0}} (\vec{v} - \vec{v}_f) \right]^2 AC_{d\infty} \frac{(\vec{v} - \vec{v}_f)}{\|(\vec{v} - \vec{v}_f)\|} \quad (11)$$

Boundary layer at the wall-fluid interface also results in a parabolic profile of blood flow (see Figure 4). The pulsative blood's velocity is modeled by an affine combination of a time-varying periodic flow with a spatial parabolic profile $p_p(\delta)$. So as to simplify the analytical expression, with no loss of generality, we only consider the first terms in the time-varying Fourier series of the physiological pulse. In the case of an artery, such an approximation leads to:

$$v_f(t) = V_f(1 + a_f \sin(\omega_f t + \phi_f))p_p(\delta) \quad (12)$$

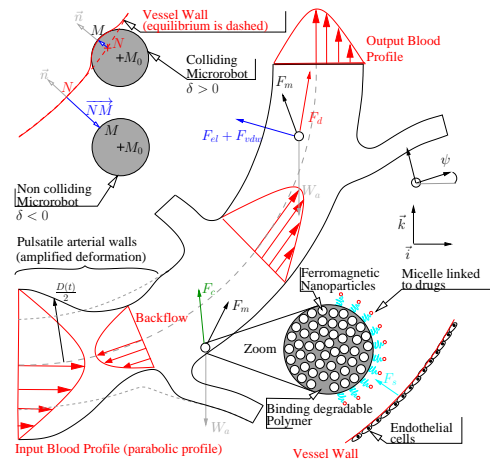


Fig. 4. Scheme of a blood vessel with minor bifurcations.

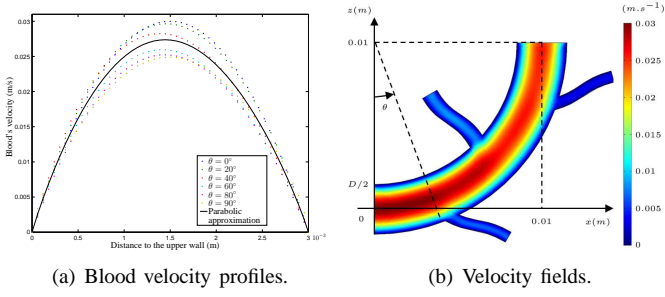


Fig. 5. CFD results of a parent vessel with minor bifurcations. (a) Blood velocity profiles: CFD results (dotted lines) and parabolic approximation (solid line). (b) Blood velocity fields: CFD results using COMSOL software.

where \vec{n} is the unit vector normal to the wall and pointing outside the vessel. Let M_0 , N and M denote respectively the center of gravity of the microrobot and its projections along \vec{n} onto the vessel wall at equilibrium and onto the microrobot's outer surface. The signed distance δ between the wall and the robot is thus defined by $\delta = \overline{NM} \cdot \vec{n}$. It should be noted that setting $a_f > 1$ in (12) results in cyclic occurrence of negative values for $v_f(t)$, what properly models the diastolic backflow occurring in arteries. Pulsatile flow caused by cardiac pumping also induces a periodic 10% deformation of the vessel diameter $D(t)$ (see Figure 4), synchronized with the blood velocity $v_f(t)$:

$$D(t) = D(1 + 0.1 \sin(\omega_f t + \phi_f)) \quad (13)$$

- **Bifurcation effects.** The velocity profile strongly depends on the geometry of the vessel. Minor bifurcations lead to slight perturbations in the velocity profile and amplitude (see Figure 5): the usual parabolic profile of the blood flow supplies a good approximation.

On the contrary, major bifurcation entails major changes (Figure 6) and the parabolic profile in (12) is no more valid. On Figure 6(a), before the apex of the bifurcation, the increase of the vessel's cross-sectional area results in skewed and flattened profiles. In the vicinity of the apex region, the velocity at the parent branch centerline promptly cancels out (from $\theta = 25^\circ$ to 30°) and the maximum

velocity is reached close to the upper wall. After the apex, the maximum velocity progressively shifts to the inner wall (see Figure 6(c)). The flow then gradually returns to a steady-state parabolic profile in the daughter branch.

Since these numerical simulations, consistent with the dedicated literature, are not compatible with real-time control constraints, it is necessary to develop analytical models of the velocity profiles that fits CFD results. Even though one can find a polynomial approximation for each angle value θ , there are two severe obstructions to such an approximation: the problem is ill-conditioned and it does not allow for a smooth change of velocity profiles as θ grows. We therefore propose a rational approximation of the blood velocity profile in the form $p_r(\delta) = a\delta^2 + b\delta + c + \frac{d\delta + e}{(\delta - p)^2 + q^2}$ and solve a well-conditioned nonlinear inverse problem for some θ values. Figure 6 shows that the interpolation results in smooth profiles that fit quite well the CFD results. Note that adding another rational fraction to $p_r(\delta)$ results in a better approximation, at the expense of a more complicated inverse problem. Since such *in-vivo* measurements are awkward, mathematical models and numerical simulations will become the main investigative tools.

- 3) **Apparent weight:** Apparent weight, i.e. combined action of weight and buoyancy, is also acting on the spherical robot:

$$\vec{W}_a = V(\rho - \rho_f)\vec{g} \quad (14)$$

where $\rho = \tau_m \rho_m + (1 - \tau_m) \rho_{poly}$ with ρ_m and ρ_{poly} the magnetic material's and polymer's densities.

- 4) **Contact force:** Since the robot moves in low velocity, the duration of the impact occurs within a few milliseconds. Hence, the contact force can be expressed by a modified Hertzian contact law [30] under the assumption of no friction between the robot and the wall during the impact:

$$\vec{F}_c = -k|\delta|^{3/2}H(\delta)\vec{n} \quad : \text{loading} \quad (15)$$

with H the Heaviside step function. Stiffness k is given by :

$$k = \frac{\frac{4\sqrt{r}}{3}}{\frac{1-\sigma_c^2}{E_c} + \frac{1-\sigma_w^2}{E_w}}$$

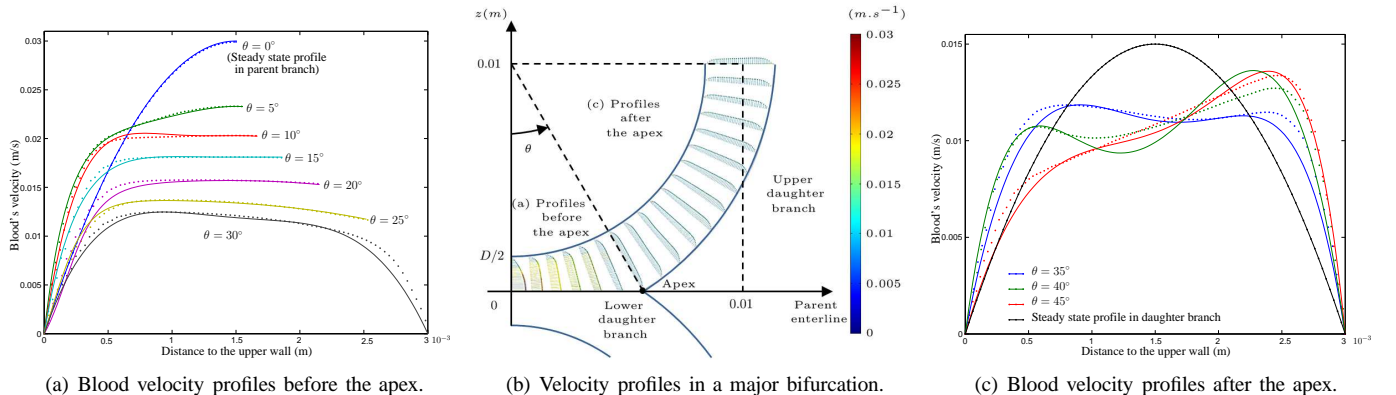


Fig. 6. CFD results of a parent vessel with a major bifurcation. (a) Blood velocity profiles before the apex: CFD results (dotted lines) and rational approximation (solid lines). (b) Blood velocity profiles: CFD results using FLUENT software. (c) Blood velocity profiles after the apex: CFD results (dotted lines) and rational approximation (solid lines).

where E_c and σ_c (respectively E_w and σ_w) are the Young's modulus and Poisson's ratio of the microrobot (respectively of the vessel wall).

The contact force during unloading is different from the one during loading and it is given by:

$$\vec{F}_c = -F_{\delta m} \left| \frac{\delta - \delta_0}{\delta_m - \delta_0} \right|^p H(\delta) \vec{n} \quad : \text{ unloading} \quad (16)$$

where $F_{\delta m}$ and δ_m are the maximum contact force and the corresponding maximum deformation of the wall. δ_0 is the permanent wall's deformation from loading/unloading cycle and exponent q belongs to $[1.5; 2.5]$.

5) *Van der Waals and electrostatic forces*: The microrobot and the wall also interact each other through van der Waals and electrostatic forces. When the microrobot is close to the wall, van der Waals force is dominant. As the robot moves away from the wall, the van der Waals force rapidly decreases and the electrostatic force prevails.

The van der Waals potential between the spherical robot and the wall is given by [31]:

$$\vec{V}_{vdw} = -\frac{A_h}{6} \left(\frac{1}{h} + \frac{1}{2+h} + \ln \frac{h}{2+h} \right) \vec{n} \quad (17)$$

where A_h is the Hamaker constant and $h = |\delta|/r$ is the normalized distance from the robot to the wall. Then, the attractive van der Waals interaction force is obtained by differentiating (17):

$$\vec{F}_{vdw} = -(\nabla \vec{V}_{vdw}) H(-\delta) \quad (18)$$

The electrostatic force between the robot and the wall considered as an uncharged surface is given by [32]:

$$\vec{F}_{el} = \frac{q^2}{4\pi\epsilon\epsilon_0(r+|\delta|)^2} H(-\delta) \vec{n} \quad (19)$$

with q the robot's charge, and ϵ_0, ϵ the vacuum and the relative blood's permittivities. [33] gives a maximum allowable charge $q(\mu C) = 4\pi r^2 \times 30(100r)^{-0.3}$ for a sphere of radius r .

6) *Steric force*: Therapeutic microrobots are generally functionalized via polymer chain grafting, e.g. doxorubicin linked via a polymeric micelle to the robot's outer wall. This polymer brush, characterized by an equilibrium length L_0 , affects the interaction of the microrobot with the endothelial glycocalyx of the vessels walls. For $0.2L_0 < |\delta| < 0.9L_0$, the repulsive interaction potential per unit area between the functionalized robot and the endothelium is given by [34]:

$$\vec{V}_{s,p/p}(z) = -\frac{25}{\pi} k_b T L_0 \tau^{\frac{3}{2}} e^{-2\pi(z/L_0)} \vec{n} \quad (20)$$

where k_b is the Boltzmann constant, T is the absolute temperature, τ is the grafting density of the polymer, z the distance between the two flat surfaces, and index p/p stands for a plane-to-plane interaction. The repulsive steric force per unit area between two flat surfaces is then deduced from (20):

$$\vec{f}_{s,p/p}(z) = -(\nabla \vec{V}_{s,p/p}) = -50k_b T \tau^{\frac{3}{2}} e^{-2\pi(z/L_0)} \vec{n} \quad (21)$$

Equation (21) is integrated using the Derjaguin approximation to infer the overall interaction between a sphere at distance

$|\delta|$ from a flat surface modeling the vessel wall:

$$\begin{aligned} \vec{F}_s(\delta) &= \vec{F}_{s,p/p}(\delta) = 2\pi r \int_{|\delta|}^{\infty} \vec{f}_{s,p/p}(z) dz \\ &= -50r L_0 k_b T \tau^{\frac{3}{2}} e^{-2\pi(|\delta|/L_0)} H(-\delta) \vec{n} \end{aligned} \quad (22)$$

B. Nonlinear Controller and Observer Design

Now, let $x_1, x_2, (x_3, x_4)$ denote respectively robot's position and velocity along \vec{i} axis (respectively along \vec{k} axis). Assuming that positions x_1 and x_3 can be measured thanks to a real-time medical imager, let y denotes the state's measure. Using expressions of forces given by (2), (11), (14), (15), (16), (18), (19), (22) and adequate projection of local frame along the geometry of the vessel, equation (1) can be written in the canonical form:

$$(\mathcal{S}) \begin{cases} \dot{X} &= Z \\ \dot{Z} &= F(X, Z) + U \\ Y &= X \end{cases} \quad (23)$$

where state vectors are given by $X = (x_1, x_3)$ and $Z = (x_2, x_4)$, the input vector $U = \frac{M}{\rho} (\nabla B_x, \nabla B_z)$ is directly related to magnetic gradients, and F is the function on \mathbb{R}^2 that stems from the projection of \vec{F}_{tot} .

Denoting $X_{ref}, \dot{X}_{ref}, \ddot{X}_{ref}$ respectively a reference trajectory, velocity and acceleration, the backstepping control law [35] for system (S):

$$U = \ddot{X}_{ref} + (k_1 + k_2)\dot{X}_{ref} + (1 + k_1k_2)X_{ref} - (1 + k_1k_2)X - (k_1 + k_2)Z - F(X, Z) \quad (24)$$

where k_1 and k_2 are the strictly positive backstepping gains, ensures the Lyapunov stabilization of the microrobot along the desired optimal trajectory (see [36] for more details).

The backstepping control law (24) requires the knowledge of the robot's velocity in addition to its position, measured by the imager. Since the velocity is not measured, we build an high gain observer to reconstruct it:

$$(\mathcal{S}') \begin{cases} \dot{\hat{X}} &= \hat{Z} + LG_x(\hat{X} - Y) \\ \dot{\hat{Z}} &= F(\hat{X}, \hat{Z}) + U + L^2G_z(\hat{X} - Y) \end{cases} \quad (25)$$

where L is the high gain, and matrices G_x, G_y are conveniently chosen [37].

III. RESULTS

The goal of the present section is to derive guidelines for optimizing the design, trajectory and control of magnetically propelled microrobots towards any bifurcation branch.

A. Model-based optimization

Limitations on the hardwares used to generate the magnetic fields and gradients induce strong restrictions on the available motive force. For BP design, the optimization is based on a maximum magnetic field gradient $\|\nabla \vec{B}\| = 80mT.m^{-1}$ available on recent clinical MRI devices, with a uniform magnetic field of amplitude $B_0 = 3T$. For EF and HT designs, we consider a maximum synchronized frequency $\frac{\omega}{2\pi} = 30Hz$ and a rotating magnetic field of amplitude $B_0 = 2mT$ [11]. To acquire results that apply for a broad range of blood vessels,

TABLE I
DIFFERENT TYPES OF BLOOD VESSEL

| Vessel | Diameter (mm) | Blood velocity (mm.s ⁻¹) |
|--------------|---------------|--------------------------------------|
| Artery | 10 | 250 |
| Small artery | 1 | 20 |
| Arteriole | 0.1 | 1 |
| Capillary | 0.01 | 0.05 |

TABLE II
PHYSIOLOGICAL PARAMETERS

| Parameter | Range |
|---------------|--|
| ε | 45 - 77 C ² .N ⁻¹ .m ⁻² |
| η | 0.008 - 0.02 Pa.s ⁻¹ |
| ρ_f | 1050.6 - 1062.1 kg.m ⁻³ |
| E_w | 1.25 - 1.37 10 ⁹ Pa |

we consider navigation through *i*) artery, *ii*) small artery, *iii*) arteriole, and *iv*) capillary. Table I presents typical diameters and blood flow velocities. To perform more realistic analysis, it is assumed that robots have a payload and polymer volumic capacity of 20% (i.e. $\tau_m = 80\%$). Materials properties are given in Table III.

We perform a model-based optimization to determine both the optimal capabilities of each robot's design and the less demanding reference trajectory so as not to reach actuators' saturations. The total force \vec{F}_{tot} an endovascular robot is subjected to is the sum of all the forces acting on the robot apart from the motive force, i.e. $\vec{F}_{tot} = \vec{F}_d + \vec{F}_{el} + \vec{F}_{vdw} + \vec{F}_s + \vec{W}_a$. Whatever the selected design (namely BP, EF or HT robot) the same external forces apply: the only difference stands in the source of their motive magnetic force \vec{F}_m (cf Section II-A). It is thus necessary to optimize both the design and the trajectory in order to maximize the ratio $\frac{F_m}{F_{tot}}$ defined by Martel in [17]. Let Δ denotes the distance between the microrobot and the vessel centerline. For each vessel, a family of non-dimensional 3D curves is drawn as a function of $\lambda = 2r/D$ (for the design optimization) and Δ (for the optimal trajectory), as shown in Figures 7(a) to 7(l). Physiological parameters' ranges, measured or estimated on patients, are given in Table II. The 3D curves may therefore differ slightly from Figures 7(a) to 7(l) depending on the parameters' values, yet the general conclusions remain valid.

1) *Design optimization*: BP, EF and HT designs can be optimized with respect to the respective sets of parameters $\{r\}$, $\{r, L, \kappa, k_\kappa, S_p\}$, and $\{r, n, \theta, \kappa\}$, so as to maximize the motive force \vec{F}_m . To compare equitably helical and elastic tail designs, we set a maximal ratio between the tail's length L and the bead's radius r corresponding to $n = 10$ helical turns for an helical tail with an optimal pitch angle $\varphi = 35^\circ$. Without violating the slender body and the small-amplitude assumptions, the elastic flagellum's radius κ and stiffness k_κ are then optimized so as to maximize the motive force (for $S_p = 3.4$). As the bead's radius r strongly affects both the motive and the total force, this optimization will result from the evolution of the ratio $\frac{F_m}{F_{tot}}$ as a function of the diameter ratio $\lambda = \frac{2r}{D}$ depicted on Figures 7(a) to 7(l).

Figures 7(a) to 7(l) depict the evolution of the ratio $\frac{F_m}{F_{tot}}$, for BP, EF and HT designs (from left to right), as they navigate in a broad range of blood vessels: from artery (Figures 7(a) to

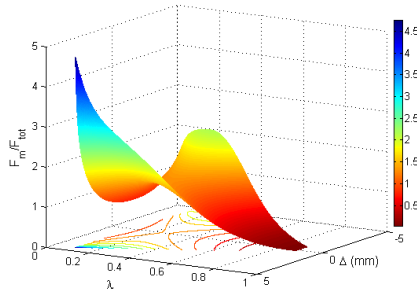
7(c)), small artery (Figures 7(d) to 7(f)) and arteriole (Figures 7(g) to 7(i)), to capillary (Figures 7(j) to 7(l)).

The drag force \vec{F}_d scales in $\sim r^2$ in large vessels and in $\sim r$ in smaller ones, where the drag (11) tends to the Stokes flow expression. Yet the motive force \vec{F}_m scales in r^3 for BP design (see (2)) and in r^2 for EF and HT designs (cf (4) and (5)). The smaller the robot's radius is, the more the drag decreases and it is even worst for the motive force. So a high radius, and in turn a high λ , improves the performances. However, drag is also affected by the partial occlusion of the vessel, through λ , which penalizes too high λ values. It results in a vessel-dependent optimal range for λ ranging from $\lambda \in [0.15; 0.55]$ in an artery to $\lambda \in [0.3; 0.6]$ in a small artery for BP design (see Figures 7(a) and 7(d)). Previous studies [17], [22] have predicted respective optimal ratios $\lambda = 0.42$ and $\lambda = 0.25$ in an artery: we show that taking advantage of the interaction forces results in a lower optimal value $\lambda = 0.15$, what reduces embolization hazards. In smaller vessels, we conversely predict almost the same profiles and optimal ratios than the ones evaluated in [22].

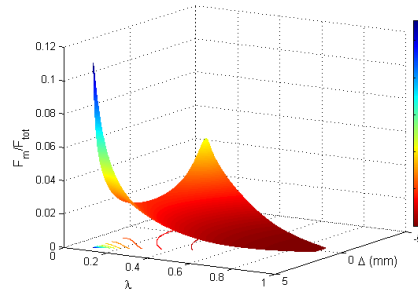
EF design does not provide enough thrust in any vessel configuration ($\frac{F_m}{F_{tot}} < 1$), even if its efficiency increases as the robot enters smaller vessels (additional studies show that EF robot can resist only a maximum $v_f = 15 \mu\text{m.s}^{-1}$ in a capillary). The same effect occurs for HT design, whose motive force also grows in r^2 , although Figures 7(i) and 7(l) illustrate that the thrust is high enough to drive such a robot in arterioles and capillaries, as emphasized in [38]. In macrovasculature, Figures 7(a) and 7(d) show that BP design is the best fitted to navigate in vessels where the drag is important, provided that the robot's trajectory is defined alongside the upper wall.

2) *Reference trajectory*: As the robot approaches the vessel's wall (as $|\Delta|$ increases), the drag force decreases because of the parabolic profile (12) of the blood flow, while interaction forces \vec{F}_{el} , \vec{F}_{vdw} and \vec{F}_s increase and can either counterbalance (for the upper wall) or amplify (for the lower wall) the apparent weight \vec{W}_a contribution. Hence, the symmetry is broken in the Δ -axis, as shown in Figure 7. Next to the upper wall, attractive interaction forces equipoise the robot's apparent weight, which minimizes the control efforts. This effect is clearly visible in arteries (Figures 7(a) to 7(f)): since blood velocity is high, drag is dominant, and it is worthwhile navigating close to the wall. In arterioles and capillaries (Figures 7(g) to 7(l)), the problem is different: blood velocity is smaller and so the drag (though higher than available motive force for BP and ET designs). Interaction forces are consequently dominant, which prevents the robot from moving in the vicinity of the wall so to benefit from a reduced drag.

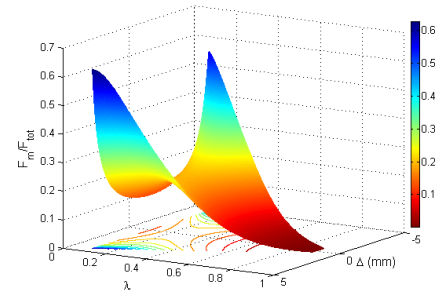
According to the forces balance presented in Section II-A and Figures 7(a) to 7(l), we can define freely the number of anchor points, e.g. four points in the present simulation. These points correspond to an optimal ratio $\frac{F_m}{F_{tot}}$, as explained in the previous section, and are distributed along the path from the start point (injection seed) to the end point (e.g. tumor target). This path has to be close to the upper vessel wall to minimize the control efforts in arteries, whereas it should be centered in smaller vessels.



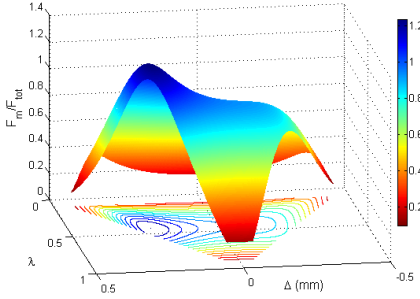
(a) Bead pulled robot in an artery



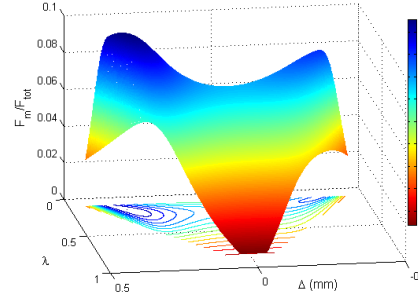
(b) Elastic flagellated robot in an artery



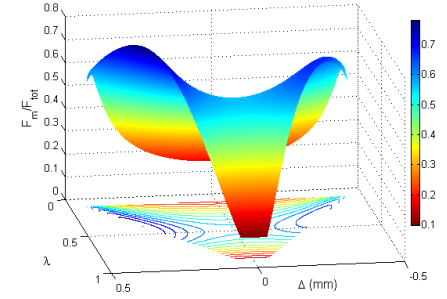
(c) Helical tailed robot in an artery



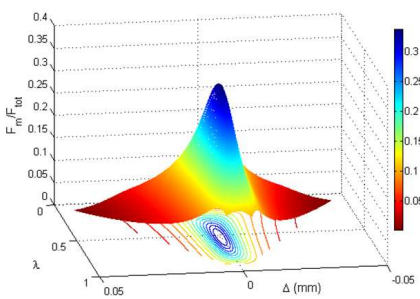
(d) Bead pulled robot in a small artery



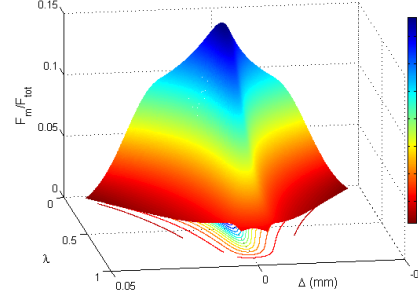
(e) Elastic flagellated robot in a small artery



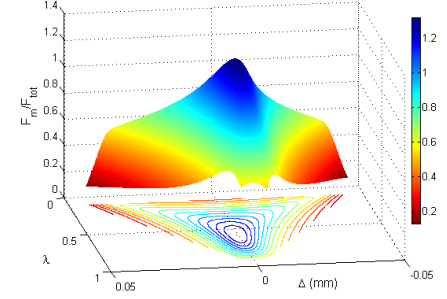
(f) Helical tailed robot in a small artery



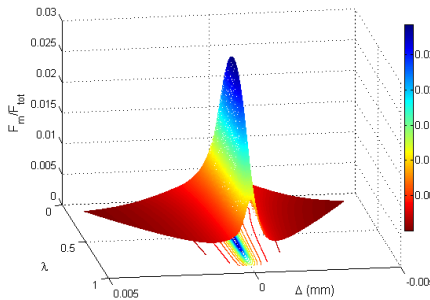
(g) Bead pulled robot in an arteriole



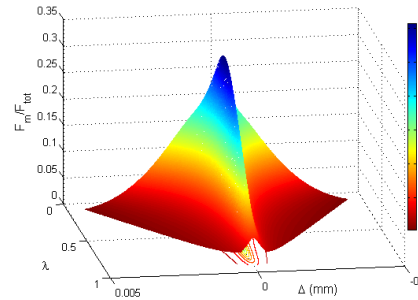
(h) Elastic flagellated robot in an arteriole



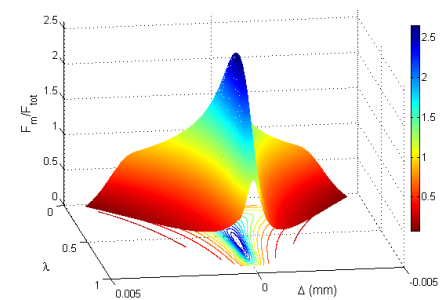
(i) Helical tailed robot in an arteriole



(j) Bead pulled robot in a capillary



(k) Elastic flagellated robot in a capillary

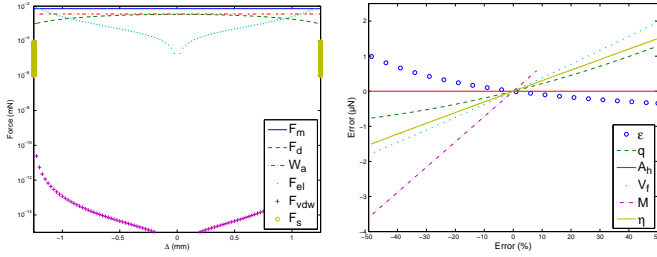


(l) Helical tailed robot in a capillary

Fig. 7. Evolution of the ratio F_m/F_{tot} as a function of λ and Δ . From left to right: bead pulled, elastic flagellated and helical tailed robots. From top to bottom, the robots navigate from artery through small artery and arterioles to capillary.

To build an optimal reference trajectory the controller can track, these anchor points have to be joined in a smooth (\mathcal{C}^2) curve. This interpolation is provided by B-splines for flexibility concerns: a change in one anchor point's position will result only in a local modification of the path, and the

reference velocity along this path can be rescaled easily. This can be of particular interest if $\frac{F_m}{F_{tot}} < 1$. For instance, figures 7(g) and 7(j) show that actual MRI devices cannot steer a BP robot in the smallest vessels because the drag force prevails. However, this limitation can be circumvented by computing a



(a) Force balance as a function to the distance to the vessel centerline. (b) Sensitivity to some uncertain parameters.

Fig. 8. (a) Force balance in a small artery. (b) Sensitivity study in a small artery.

reference trajectory so as to synchronize the reference velocity with the blood flow.

B. Force balance and sensitivity study

The force balance plotted on Figure 8(a) for a small artery shows that the steric and van der Waals interactions can be omitted if considering the control of a microcarrier in large vessels, since they are respectively around 3 and 6 orders of magnitude under other forces. It is nonetheless necessary to take it into account in small arterioles and capillaries where they impact severely the force balance. Since the proposed model involves numerous uncertain parameters, a sensitivity study is also performed on Figure 8(b). The force balance is highly sensitive —linearly— to magnetization M , and —nonlinearly— to blood permittivity ε , charge q , blood velocity V_f . We have already showed in [39] that such uncertainties on linear parameters like M or $\frac{q^2}{\varepsilon}$ can be successfully addressed using adaptive backstepping.

C. Simulation results

The following simulation is performed by taking into account some limitations of a clinical MRI system. The magnetic field is strong enough (3T) to assume that the particles reach their saturation magnetization. In order not to exceed the capacity of MRI systems, the applied control law is now corrected as $U_a(t) = \frac{U(t)}{k(t)}$ with $k(t) = \max\left(1, \frac{U(t)}{U_{sat}}\right)$ and a $100 \text{ mTm}^{-1}\text{s}^{-1}$ slew rate.

The studied artery's radius is around 1.5 mm and exhibits some minor and one major bifurcation. The most effective design is thus BP design (Figure 7(d)), and the optimal reference trajectory is set near the outer wall, as stated in Section III-A2. The radius of the robot is hence set to $250 \mu\text{m}$ so as to respect the optimal ratio $\lambda = 0.15$, as stated in Section III-A1. Performances and stability of the controller with respect to noise measurement and parameters uncertainties are now illustrated by a closed-loop simulation, whose nominal parameters are given in Table III.

MRI and computed tomography devices currently have a spatial resolution around some hundreds of micrometers. Besides, since the microrobot is composed of a ferromagnetic nanoparticles aggregate, it induces artifacts on the imager of the MRI device. Hence we suppose that the position

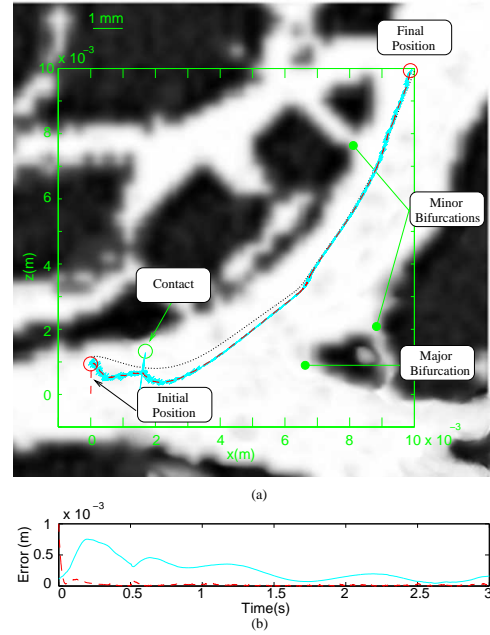


Fig. 9. (a) XZ trajectory: reference trajectory (black dotted line), robot's trajectory (blue solid line) and estimated trajectory (red dashed line). (b) Error: tracking error (blue solid line) estimation error (red dashed line)

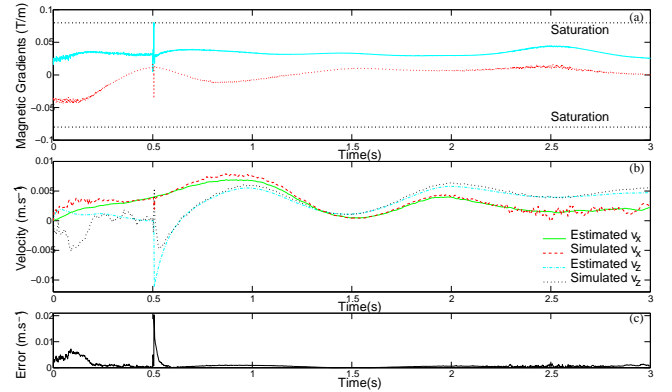


Fig. 10. (a) Control inputs: magnetic field gradients on \vec{r} -axis (red) and on \vec{k} -axis (blue). (b) Simulated and estimated velocities along \vec{r} and \vec{k} -axes. (c) Velocity estimation error.

measurement is with an accuracy to within $100 \mu\text{m}$ (i.e 10% of the measured signal), modeled by a white gaussian noise. Moreover, we assume that a 5% uncertainty affects the blood velocity, what models the modeling errors generated by *i*) the presence of minor bifurcations, *ii*) errors related to the approximation of CFD velocity profiles by a rational profile, and *iii*) the difficulty to estimate correctly the blood velocity.

Figure 9 (a) illustrates that the proposed controller-observer is stable. After the transient phase and despite the $100 \mu\text{m}$ noise amplitude, the estimation error (Figure 9 (b)) is smaller than $10 \mu\text{m}$ (i.e. 10% of nominal value). During the convergence of the observer, within $t = 0 \text{ s}$ and $t = 0.2 \text{ s}$, the tracking error (Figure 9 (b)) increases. After this transient phase, one can notice that the observer reconstructs correctly the state. At $t = 0.5 \text{ s}$, important aberrant values are injected in the imaging measurements to test the robustness of the controller-observer

TABLE III
SIMULATIONS DATA

| | | |
|---|-------------------------|-------------------------------|
| Plasma viscosity | η_{pl} | $5 \cdot 10^{-3} [Pa.s]$ |
| Blood density | ρ_f | $1060 [kg.m^{-3}]$ |
| Magnetic material density | ρ_m | $7874 [kg.m^{-3}]$ |
| Polymer density | ρ_{poly} | $1500 [kg.m^{-3}]$ |
| Magnetic ratio | τ_m | 0.8 |
| Vessel diameter | D | $3 \cdot 10^{-3} [m]$ |
| Robot's radius | r | $250 \cdot 10^{-6} [m]$ |
| Equilibrium length | L_0 | $100 \cdot 10^{-9} [m]$ |
| Magnetization | M | $1.72 \cdot 10^6 [A.m^{-1}]$ |
| Young's moduli | E_c, E_w | $10^9, 10^9 [Pa]$ |
| Poisson's ratios | σ_c, σ_w | 0.27, 0.2 |
| Hamaker constant | A_h | $4 \cdot 10^{-19} [J]$ |
| Blood permittivity | ϵ | $70 [C^2.N^{-1}.m^{-2}]$ |
| Blood velocity parameters | V_f | $0.025 [m.s^{-1}]$ |
| | a_f, w_f, ϕ_f | $1.15, 2\pi, \frac{\pi}{2}$ |
| Initial condition on X, Z | X_0, Z_0 | $(0, 0.001)^T, (0, 0)^T$ |
| Initial condition on \dot{X}, \dot{Z} | \dot{X}_0, \dot{Z}_0 | $(0, 0)^T, (0, 0)^T$ |
| Inputs saturations | U_{sat} | $80 \cdot 10^{-3} [T.m^{-1}]$ |
| Controller gains | k_1, k_2 | 5, 10 |
| Observer gains | L, g_1, g_2, g_3, g_4 | 5, -6, -13, -12, -4 |

pair to bounded disturbances. It causes the microrobot to collide with the wall and the control inputs reach the actuator saturation (Figure 10 (a)), but the controller quickly rejects the disturbance to track the reference trajectory. After $t = 0.6s$, despite noise measurement and modeling error, the tracking is efficient and the error does not exceed $150\mu m$. This is an excellent result since the model is very sensitive to errors on blood's velocity.

D. Discussion

The dynamic behaviour of the robot in blood vessels is highly affected by various physiological parameters (see Table II and Figure 8), e.g. the blood relative permittivity ϵ , viscosity η , density ρ_f , etc. These parameters may vary with respect to many other factors such as temperature, patient age and health, etc... The selected control approach must be sufficiently robust to these parameters uncertainties to track correctly the pre-planned reference trajectory. Even though *off-line* identification of some biological parameters is a solution, *in-vivo* estimation remains a difficult issue. That is why we have developed an adaptive control [39] to *on-line* estimate some physiological parameters, which greatly improves the robustness to modeling errors on linear parameters. The estimation of non-linearly varying parameters requires further study and remains an outstanding problem.

Poor performances of EF design should be compared to the maximum velocity that other similar designs can reach within the same constraints: $4\mu m.s^{-1}$ for a paramagnetic beating flagellated robot [12], $30\mu m.s^{-1}$ for E. Coli, and over $200\mu m.s^{-1}$ for magnetotactic bacteria [7]. In the last two cases, the improved efficiency is a result of the distributed actuation in natural flagella. The shape anisotropy and flagellum design of both EF and HT designs make it difficult to *i)* manoeuvre in vessels and anticipate wall interactions with the tail, and to *ii)* consider a progressive downscaling so as to benefit from an optimal ratio while navigating from macro to microvasculature. Since such designs are well suited

for exploring small vessels, it is tempting to embed such $5\mu m$ devices inside a bigger agglomerate. The latter could be bead pulled in arteries, then break down to release the flagellated microrobots in the arterioles. However such a design requires both strong magnetic gradients and oscillating magnetic field: in any case, a clinical MRI device cannot fulfill these requirements.

Spatial resolution of current medical imagers is an important limitation, especially within real-time constraints [1], [3]. However, future imagers like 7T MRI or 256 slice computed tomography devices are promising for high spatial and temporal resolution imaging. This will be a key point for implementing targeted minimally invasive therapies using microrobots that require to navigate into smaller vessels. Using an MRI device to provide both imaging and thrust also requires multiplexing approach, what induces both a lower imaging resolution and a degraded tracking during imaging period [23]. Imaging post-processing—notably time required to perform accurate localization of the microrobot using its magnetic signature despite a size below the MRI resolution [40]—and delays can also severely degrade the proposed approach. A way to overcome these downsides is either to upgrade the MRI devices with additional gradient coils, either to use an additional device (stereotactic device from Stereotaxis company www.stereotaxis.com, or Octomag device from Aeon Scientific www.aeon-scientific.com) inside the imager for propulsion purpose. Slowing down the reference trajectory may also reduce discrepancies induced by imaging delays. However, addressing properly stability concerns induced by delays requires a Lyapunov-Razumikhin/Krasovskii based backstepping.

Controlling such microrobots in the vasculature raises safety concerns. The two main limitations are inadequate embolization and magnetic hazards. Designing the microrobot as a degradable polymer aggregate is an answer to the first issue. Using time-varying magnetic fields can induce neurostimulation: at the present time, there are no worldwide regulations for time-varying magnetic gradients. Our works consequently deal with standard slew rates available on clinical MRI devices.

We approximate the blood velocity given by CFD results by analytical functions for quite simple vascular geometry. A more generic and robust approach relies on the design of an observer of the blood velocity, i.e. on an *on-line* estimation of the blood flow from the microrobot's position and heartbeat measurements, which is still an open problem.

IV. CONCLUSION

This paper proposes a physics-based modeling framework to optimize the navigation of magnetically guided therapeutic microrobots in blood vessels. The robot consists of a polymer binded aggregate of nanosized ferromagnetic particles grafted with micelles to drugs. The model of the robot takes into account wall effects, wall interactions and non-Newtonian behaviour of blood. The benefits of using a model based approach are illustrated through the definition of both an optimal size of the microrobot and an optimal trajectory so as to minimize the control efforts. The proposed optimization

framework makes it possible to generalize the navigation process to complex vasculature networks. Taking into account the geometry of the vessels, the blood flow velocity at bifurcations and blood properties, we can optimize targeting with an appropriate backstepping control law coupled with a high gain observer. The performances and robustness of the approach are validated by simulation results including noise, disturbances, and model parameters uncertainties.

REFERENCES

- [1] S. Achenbach, D. Ropers, A. Kuettner, T. Flohr, B. Ohnesorge, H. Bruder, H. Theessen, M. Karakaya, W. G. Daniel, W. Bautz, W. A. Kalender, and K. Anders, "Contrast-enhanced coronary artery visualization by dual-source computed tomography: initial experience," *European Journal of Radiology*, vol. 57, no. 3, pp. 331–335, 2006.
- [2] M. Uecker, S. Zhang, D. Voit, A. Karas, K.-D. Merboldt, and J. Frahm, "Real-time mri at resolution of 20 ms," *NMR in Biomedicine*, vol. 23, pp. 986–994, 2010.
- [3] S. Zhang, N. Gersdorff, and J. Frahm, "Real-time magnetic resonance imaging of temporomandibular joint dynamics," *The Open Medical Imaging Journal*, vol. 5, pp. 1–7, 2011.
- [4] R. McNeil, R. Ritter, B. Wang, M. Lawson, G. Gillies, K. Wika, E. Quate, M. Howard, and M. Grady, "Functional design features and initial performance characteristics of a magnetic-implant guidance system for stereotactic neurosurgery," *IEEE Transactions on Biomedical Engineering*, vol. 42, no. 8, pp. 793–801, 1995.
- [5] F. Carpi and C. Pappone, "Magnetic manoeuvring of endoscopic capsules by means of a robotic navigation system," *IEEE Transactions on Biomedical Engineering*, vol. 56, no. 5, pp. 1482–1490, 2009.
- [6] M. Sitti, "Miniature devices: Voyage of the microrobots," *Nature*, vol. 458, pp. 1121–1122, April 2009.
- [7] S. Martel, M. Mohammadi, O. Felfoul, Z. Lu, and P. Pouponneau, "Flagellated magnetotactic bacteria as controlled mri-trackable propulsion and steering systems for medical nanorobots operating in the human microvasculature," *International Journal of Robotics Research*, vol. 28, pp. 571–582, 2009.
- [8] T. Honda, K. I. Arai, and K. Ishiyama, "Micro swimming mechanisms propelled by external magnetic fields," *IEEE Transactions on Magnetics*, vol. 32, no. 5, 1996.
- [9] B. J. Nelson, I. Kaliakatsos, and J. Abbott, "Microrobots for minimally invasive medicine," *Annual Review of Biomedical Engineering*, vol. 12, pp. 55–85, 2010.
- [10] J. Edd, S. Payen, B. Rubinsky, M. L. Stoller, and M. Sitti, "Biomimetic propulsion for a swimming surgical microrobot," *IEEE International Conference on Intelligent Robots and Systems, Las Vegas*, pp. 2583–2588, 2003.
- [11] L. Zhang, K. E. Peyer, and B. J. Nelson, "Artificial bacterial flagella for micromanipulation," *Lab on a chip*, vol. 10, no. 17, pp. 2203–2215, 2010.
- [12] R. Dreyfus, J. Beaudry, M. L. Roper, M. Fermigier, H. A. Stone, and J. Bibette, "Microscopic artificial swimmers," *Nature*, vol. 437, pp. 862–865, October 2005.
- [13] C. H. Wiggins, R. Riveline, A. Ott, and R. E. Goldstein, "Trapping and wiggling: Elastohydrodynamics of driven microfilaments," *Biophysical Journal*, vol. 74, pp. 1043–1060, February 1998.
- [14] A. A. Evans and E. Lauga, "Propulsion by passive filaments and active flagella near boundaries," *Phys. Rev. E*, vol. 82, no. 4, p. 041915, 2010.
- [15] H. Choi, J. Choi, S. Jeong, C. Yu, J. O. Park, and S. Park, "Two-dimensional locomotion of a microrobot with a novel stationary electromagnetic actuation system," *Smart Material and Structures*, vol. 18, p. 115017, 2009.
- [16] S. Floyd, C. Pawashe, and M. Sitti, "Two-dimensional contact and non-contact micromanipulation in liquid using untethered mobile magnetic microrobot," *IEEE Transactions on Robotics*, vol. 25, no. 6, pp. 303–308, 2009.
- [17] J.-B. Mathieu, G. Beaudoin, and S. Martel, "Method of propulsion of a ferromagnetic core in the cardiovascular system through magnetic gradients generated by an mri system," *IEEE Transactions on Biomedical Engineering*, vol. 53, no. 2, pp. 292–299, 2006.
- [18] S. Martel, J.-B. Mathieu, O. Felfoul, A. Chanu, E. Aboussouan, S. Tamaz, P. Pouponneau, H. Yahia, G. Beaudoin, G. Soulez, and M. Mankiewicz, "Automatic navigation of an untethered device in the artery of a living animal using a conventional clinical magnetic resonance imaging system," *Applied Physics Letters*, vol. 90, no. 11, 2007.
- [19] J. J. Abbott, O. Ergeneman, M. P. Kummer, A. M. Hirt, and B. J. Nelson, "Modeling magnetic torque and force for controlled manipulation of soft-magnetic bodies," *IEEE Transactions on Robotics*, vol. 23, no. 6, 2007.
- [20] H. Li, J. Tan, and M. Zhang, "Dynamics modeling and analysis of a swimming microrobot for controlled drug delivery," *IEEE Transactions on Automation Science and Engineering*, vol. 6, no. 2, pp. 220–227, 2009.
- [21] C. Pawashe, S. Floyd, and M. Sitti, "Modeling and experimental characterization of an untethered magnetic micro-robot," *International Journal of Robotics Research*, vol. 28, no. 8, pp. 1077–1094, 2009.
- [22] P. Vartholomeos and C. Mavroidis, "Simulation platform for self-assembly structures in mri-based nanorobotic drug delivery systems," *IEEE International Conference on Robotics and Automation*, pp. 5594–5600, 2010.
- [23] S. Tamaz, R. Gourdeau, A. Chanu, J.-B. Mathieu, and S. Martel, "Real-time mri-based control of a ferromagnetic core for endovascular navigation," *IEEE Transactions on Biomedical Engineering*, vol. 55, no. 7, 2008.
- [24] H. Choi, J. Choi, K. Cha, L. Quin, J. Li, J. O. Park, S. Park, and B. Kim, "Position stabilization of microrobot using pressure signal in pulsating flow of blood vessel," *IEEE Sensors 2010 conference*, vol. 18, pp. 723–726, 2010.
- [25] Y.-W. Jun, J.-W. Seo, and J. Cheon, "Nanoscaling laws of magnetic nanoparticles and their applicabilities in biomedical sciences," *Accounts of Chemical Research*, vol. 41, no. 2, pp. 179–189, 2008.
- [26] J. J. Abbott, K. E. Peyer, M. C. Lagomarsino, L. Zhang, L. X. Dong, I. K. Kaliakatsos, and B. J. Nelson, "How should microrobots swim?" *International Journal of Robotics Research*, vol. 28, pp. 1434–1447, 2009.
- [27] B. Behkam and M. Sitti, "Design methodology for biomimetic propulsion of miniature swimming robots," *ASME Journal of Dynamic Systems, Measurement, and Control*, vol. 128, no. 1, 2006.
- [28] A. R. Pries, T. W. Secomb, and P. Gaetgens, "Biophysical aspects of blood flow in the microvasculature," *Cardiovascular Research*, vol. 32(4), pp. 654–667, 1996.
- [29] R. Kehlenbeck and R. D. Felice, "Empirical relationships for the terminal settling velocity of spheres in cylindrical columns," *Chemical Eng. Technology*, vol. 21, pp. 303–308, 1999.
- [30] I. Choi and C. Lim, "Low-velocity impact analysis of composite laminates using linearized contact law," *Composite Structures*, vol. 66, pp. 125–132, 2004.
- [31] K. Iimura, S. Watanabe, M. Suzuki, M. Hirota, and K. Higashitani, "Simulation of entrainment of agglomerates from plate surfaces by shear flows," *Chemical Engineering Science*, vol. 64, pp. 1455–1461, 2009.
- [32] D. Hays, "Electrostatic adhesion of non-uniformly charged dielectric spheres," *Institute of Physics Conference Series*, vol. 118, pp. 223–228, 1991.
- [33] —, *Role of Electrostatics in Adhesion, in Fundamentals of Adhesion*, L.-H. Lee, Ed. Plenum Press, 1991.
- [34] H. J. Butt, M. Kappl, H. Mueller, R. Raiteri, W. Meyer, and J. R uhe, "Steric forces measured with the atomic force microscope at various temperatures," *Langmuir*, vol. 15, no. 7, pp. 2559–2565, 1999.
- [35] I. Kanellakopoulos, P. Kokotović, and A. Morse, "A toolkit for nonlinear feedback design," *Systems and Control Letters*, vol. 18, pp. 83–92, 1992.
- [36] L. Arcese, A. Cherry, M. Fruchard, and A. Ferreira, "Dynamic behavior investigation for trajectory control of a microrobot in blood vessels," *IEEE International Conference on Intelligent Robots and Systems*, pp. 5774–5800, 2010.
- [37] J. Gauthier, H. Hammouri, and S. Othman, "A simple observer for nonlinear systems. application to bioreactors," *IEEE Transactions on Automatic Control*, vol. 37, no. 6, pp. 875–880, 1992.
- [38] J. Abbott, Z. Nagy, F. Beyeler, and B. Nelson, "Robotics in the small: Part 1 microrobotics," *IEEE Robotics and Automation Magazine*, vol. 14, no. 2, pp. 92–103, June 2007.
- [39] L. Arcese, M. Fruchard, F. Beyeler, A. Ferreira, and B. J. Nelson, "Adaptive backstepping and mems force sensor for an mri-guided microrobot in the vasculature," *IEEE International Conference on Robotics and Automatics*, pp. 4121–4126, 2011.
- [40] E. Shapiro, S. Skrtic, K. Sharer, J. M. Hill, C. E. Dunbar, and A. P. Koretsky, "Mri detection of single particles for cellular imaging," *Proceedings of the National Academy of Sciences of the United States of America*, vol. 101, no. 30, pp. 10901–10906, 2004.